communications physics

ARTICLE

https://doi.org/10.1038/s42005-023-01203-2 OPEN

Introducing field evaporation energy loss spectroscopy

Loïc Rousseau [1✉], Antoine Normand[1], Felipe F. Morgado[2], Hanne-Sofie Marie Scisly Søreide[3], Leigh T. Stephenson [2], Constantinos Hatzoglou[3], Gérald Da Costa[1], Kambiz Tehrani[4], Christoph Freysoldt [2], Baptiste Gault [2,5] & François Vurpillot [1]

Retrieving information on the chemical and bonding states of atoms in a material in three-dimensions is challenging even for the most advanced imaging techniques. Here, we demonstrate that this information is accessible via straight-flight-path atom probe tomography experimental data, however it requires additional processing. Using an activation energy model that involves linear field dependance, and complementing it with DFT simulations, we extract the ion energy loss related to the kinetics of the field evaporation process from the mass peak shape. In turn, we reconstruct how evaporated atoms were originally bound to the surface. We name our data processing approach evaporation energy loss spectroscopy (FEELS), and showcase its application by analyzing microstructural features and defects in an array of metallic materials. Finally, we discuss the general applicability of FEELS to any atom probe data set.

[1] Groupe de Physique des Matériaux, UMR6634 CNRS, Université de Rouen, Saint-Etienne-du-Rouvray 76800 Normandie, France. [2] Max-Planck Institut für Eisenforschung GmbH, Organization, Düsseldorf D-40237, Germany. [3] Department of Materials Science and Engineering, Norwegian University of Science and Technology, Trondheim 7491, Norway. [4] ESIGELEC, Saint-Etienne-du-Rouvray 76800 Normandie, France. [5] Department of Materials, Royal School of Mines, Imperial College London, London SW 2AZ, UK. ✉email: loic.rousseau.27@gmail.com

There is a gap in the cornucopia of microscopy and microanalysis techniques to achieve a three-dimensional technique able to access the binding state of atoms with a resolution better than a nanometer. We introduce here a data-analysis approach that makes it easier to quantify the activation kinetics of field evaporation, in the low-activation-energy regime where voltage-pulsed atom-probe tomography (VPAPT) takes place. If a further theory can be put in place that quantitatively links these activation-related parameters to parameters relating to surface-atom binding, as we firmly hope, then it will become possible to extract surface-binding-related information from APT measurements. For the time being this is a topic for ongoing research, but our new data-analysis approach will enable the building-up of relevant databases.

APT uses an intense electrostatic field generated at the apex of a sharp needle-shaped specimen to locally break atomic bonds between surface atoms, allowing precise control of their removal[1]. The atoms constituting the material itself are thus ionized and projected by the divergent electrostatic field, and collected by a position- and time-sensitive single-particle detector. Post-processing algorithms are used to assign an elemental nature to each ion using time-of-flight mass spectrometry (TOF-MS) and to reconstruct a 3D near-atomic scale map of the field evaporated volume[2,3]. APT allows compositional analysis of individual microstructural features with a high sensitivity[4].

However, strong differences in the surface atoms' binding strength change the electrostatic field required for their field evaporation. Hence, it alters the sequences in which the atoms are removed[1] and mesoscale changes in the specimen shape that lead to trajectory aberrations[5–8], reconstruction artefacts[9], and species-specific losses due to preferential field evaporation of a species[10–12]. Those effects combine to limit the ultimate spatial resolution of the technique[7,13–18] and to prevent the direct imaging of the complete crystalline lattice[14,19–21]. Field evaporation has been studied extensively in the past[22,23] for the possible ability to measure directly and locally binding energy of single adatoms (i.e. an isolated atom in contact with the surface of a crystal) Early experimental efforts were based on measurements of the applied desorption field strengths and comparisons to desorption models. In practice, the local surface field is a difficult experimental parameter to measure since the surface reorganizes itself under field evaporation conditions. The electrostatic field is measured indirectly using average values derived from the applied voltage hinders the derivation of the binding energies that are related to the local atomic environment and curvature[24]. By following the sequence of field evaporation, some local information on the binding nature of atoms was achieved experimentally by Boll et al.[25]. However, only a few examples have been presented, due to the complexity of the method[26]. Besides these methods based on the observation of the field evaporation behavior, Ernst and coworkers[27] proposed to measure directly the absolute energy of field-evaporated atoms using retarding potential experiments. Binding energies of surface atoms under the presence of a high field were accurately measured[28], but the apparatus can not be used simultaneously with three-dimensional reconstruction from APT measurements.

Recent studies[29–31] have proposed the use of multiple field evaporation events to infer bonding mechanisms in thermoelectric and phase change materials, but APT cannot readily inform on the energetics of atomic bonds inside the material itself, merely at its surface under an intense electrostatic field. After data mining, the spatial resolution at the near-atomic scale is also lost and the relationship between the chemical state of an atom and its field evaporation behavior cannot be readily determined.

Correlative workflows enable to combine APT composition measurements with structural and chemical analyses using (scanning) transmission electron microscopy ((S)TEM). (S)TEM can retrieve grain orientations, the structure of interfaces or complex phases, structural defects such as interfaces, dislocations, slip bands, or stacking faults[32], as well as direct probing of physical properties[33,34]. Spectroscopy of the energy lost by the electrons exiting the imaged specimen (electron energy loss spectroscopy—EELS) provides chemical information in a two-dimensional projection through the specimen thickness, with a resolution approaching single-atomic columns. Contrary to APT, EELS provides direct information on inter-atomic bonding or on local modes of electronic or phonon vibration inside the observed thin section of the material[35,36]. Nevertheless, the chemical sensitivity of (S)TEM-based methods is only around 1 at.%[36], and the projected image makes the precise analysis of small microstructural features embedded in a matrix challenging.

Here, we showcase how APT has the promise of bringing insights into the binding of surface atoms in field evaporation conditions by reprocessing existing datasets. Please note that, herein, the term APT only refers to the voltage pulse straight-flight-path instruments without ion optical devices (e.g. a reflectron)[37–40]. This is because any energy compensation[41–43] interfering with the ions trajectories suppresses this information related to the energy deficits (i.e. mass peak tail) induced by nanosecond voltage pulses.

From the physics of field evaporation, we derive a parameter (with the dimensions of energy) that relates to the rate-of-change of activation energy Q with field F, when the activation energy is close to zero and Q can be considered a linear function of F. We call this the C-value. We assume that, when appropriate linking theory is in place, this C-value will be able to inform on the energetics of local surface atomic neighborhoods that can be mapped in 3D at the nanometer scale. As already indicated, the development of reliable linking theory is an ongoing research problem. For clarity, we note that the C-value is different from the sublimation energy. Physically, in simple pictures of field evaporation, the C-value and the field evaporation activation energy from which it is derived can be seen as related to the energy needed to stretch and break the bond between the field-evaporated atoms and their first nearest neighbors. Making reliable experimental determinations of C-values is a first step towards APT investigations of surface-bonding energetics, and these determinations can be done more successfully and more easily by FEELS than by earlier methods. We report the application of FEELS to pure metals and metal alloys, including structural defects, to demonstrate that useful and potentially highly important determinations of C-values can be made. Hopefully, future theoretical advances will show definitively that these C-values can be reliably converted to provide a three-dimensional mapping of C-value variations at the nanoscale, unlocking other ways for advancing the understanding of structure-property relationships in a wide range of materials.

Results

Sublimation energy, binding energy of surface atoms under electrostatic field, and field evaporation process. Prior to field evaporating, a surface atom is partially charged, in accordance with Gauss' theorem. Under field evaporation conditions, a surface atom (named an "adatom" in this paper) is initially bound with a certain binding energy close to the sublimation energy Λ. State-of-the-art models for field evaporation interpret the transition from a surface-bound atom to a departed and projected ion as a thermodynamic process. At cryogenic temperature $T = 20-100$ K, the atom overcomes an energy barrier of a few

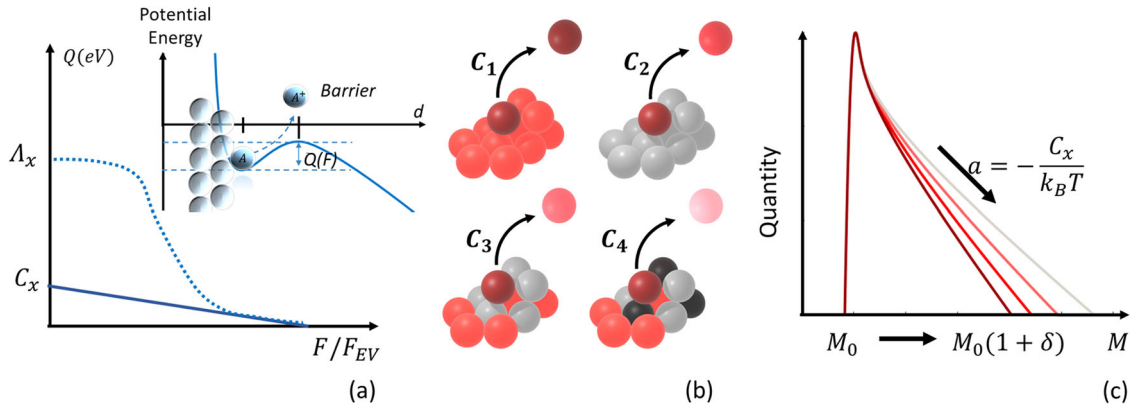

Fig. 1 Qualitative representation of the field evaporation process of a surface atom. a Field evaporation principle of a surface atom and qualitative representation of the field evaporation energy barrier evolution as a function of the field. **b** Qualitative representation of field evaporation of an atom depending on the surface structure. C_1: the configuration corresponds to a pure material. C_2: the configuration corresponds to a solute atom in a matrix. C_3: the configuration corresponds to a binary structure. C_4: The configuration corresponds to a ternary structure. The list of configurations is none exhaustive. **c** Qualitative form of the corresponding mass peak to the field evaporation sequence. The mass peak tail involves a function of the energy deficit δ induced by the voltage pulse. The mass peak presents a linear tail in log scale with a slope factor of $a = -C_x/k_BT$. In this example, a depends on the parameter C_x since the temperature T is considered constant. We consider C_1 (dark red) > $C2$ (red) > $C3$ (light red) > C_4 (pink).

tenths of an electron volt, lowered by the intense electrostatic field F[44].

Current calculation methods[45–49] based on density-functional theory (DFT) or molecular dynamics (MD) demonstrate that the complete assessment of the evolution of this energy barrier as a function of the applied field, noted $Q(F)$, is possible but remains challenging. Indeed, the relaxation of surface atom positions under the strong stress of the Maxwell forces induced by the surface field is necessary at each step of the computation[46]. Nevertheless, current DFT-based models now reproduced a near quantitative evolution of the energetic of the first step of field evaporation on various metal surfaces and atomic arrangements. The barrier, $Q(F)$, becomes 0 with the application of a sufficient surface electrostatic field referred to as the zero barrier evaporation field (ZBEF) F_{EV}, which is dependent on the elemental nature of the field evaporating atom and its direct surrounding neighbors (Fig. 1). Our DFT-based calculation[46,48] suggest that the evaporation is a universal mechanism governed by a two-stage process: a rollover event, followed by the actual departure from the surface. Each of these stages has its own energy barrier. At a high field ($F > 0.85F_{EV}$), the rollover is predominant. The adatom travels to a departing site, where it experiences a much lower field evaporation barrier. During this process, the energy follows a smooth bond-stretching trend governing the evolution of the energy barrier as a function of the displacement of the adatom. Surprisingly, for the small Q-values applicable to the VPAPT regime (Fig. 1a), the evolution of the energy barrier $Q(F)$ can be well approximated by a linear function (Eq. (1))[46,49]. The slope of the decay depends directly on the shape and size of the barrier encountered by the field evaporating atoms, which means that this decay is an indirect assessment of how strongly adatom is bound to its first neighbors during its displacement on the surface. This two-stage process was postulated as early as 1974[50] and an analytical model was proposed by Wada[51]. In Wada's interpretation the zero-field barrier energy is simply the difference in binding energies between the kink-site position and the position after the field-induced roll-over, which agrees with recent atomistic simulations[48] During APT measurement, the specimen is maintained at a cryogenic temperature $T < 100$ K and atoms are removed from the surface by an applied electrostatic field very close to the ZBEF ($F > 0.85F_{EV}$)[44]. The field is generated by a high DC voltage applied on the sharp needle and the atom's bond breaking is triggered by a high nanosecond voltage pulse with an amplitude of 10−25% of the DC voltage applied on the counter electrode. The field evaporation sequence follows an Arrhenius law Φ (Eq. (1)) that is dependent on the energy barrier $Q(F)$ and the temperature of analysis T[1].

Non-linearities of $Q(F)$ linked to the path of the adatom at the surface during the escaping process were reported experimentally[51] and predicted[45–49], but only under a low field ($F < 0.85F_{EV}$), which is not typically used in APT experiments, even at the applied DC-voltage (Fig. 1).

$$\begin{cases} Q(F) = C\left(1 - \frac{F}{F_{EV}}\right) \\ \Phi \propto \exp\left(\frac{-Q(F)}{k_B T}\right) \end{cases} \quad (1)$$

Experimentally, only measurements of the energy barrier evolution as a function of the flux were reported for W[52]. By precisely measuring the evaporation flux Φ as a function of the specimen base temperature T and the applied field F, both studies show linear decrease of $Q(F)$ as predicted by DFT[46]. The linearity of the energy barrier as a function of the applied field is expected in most of materials, as indirectly observed in field ion microscopy[51]. However, since there are no quantitative experimental data available on Al, we also performed a series of APT experiments for temperatures from 25 to 100 K to verify the linearity of $Q(F)$ (Supplementary Note 1).

From a linear plot of $Q(F)$, we can identify the parameter C in Eq. (1) as the slope of this plot. Estimates of C have previously been made by measuring FEV fluxes or rate-constant. However, such methods have several limits. They require dedicated and meticulous experiments and are only applicable to pure metals and the user must consider variations from one specimen to another. We, therefore, looked for alternatives to evaluate the parameter C. In APT, it is commonly assumed that the ions leave at the maximum of the voltage pulse and are nearly instantaneously accelerated to their final velocity to be collected by the spatial and time-sensitive detector. The ion time-of-flight is calculated and the energy conservation law is therefore used to define the mass-to-charge ratio of the species and plot the corresponding mass peaks[2] (Supplementary Note 2).

In reality, atoms are field evaporated following the Arrhenius law (Eq. (1)) and thus the majority leave around the maximum of the voltage pulse with a small energy deficit δ[53]. Consequently, the

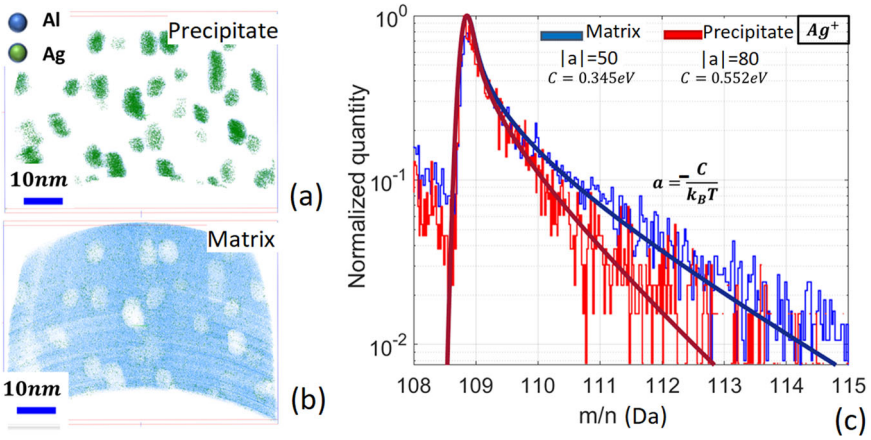

Fig. 2 Experimental measurement of the *C*-value in AlAg analyzed at $T = 80$ K with a pulse fraction of 20%. a Visualization of the AlAg precipitate. **b** Al matrix with a residual amount of Ag (<2%). **c** Evaluation of the mass peak tail slope factor (Supplementary Note 2) (blue). The value of the slope factor $a = -50$ gives a $C = 0.345$ eV for Ag atoms in the matrix (red). The value of the slope factor $a = -80$ gives a $C = 0.552$ eV for Ag atoms in the precipitates.

evolution of the mass-to-charge M with respect to the expected value M_0 for the isotopic mass of the known elements can be directly provided by the estimation of δ (Fig. 1), since this error is larger than any other sources of errors such as uncertainty on the time or length measurements[53]. This leads to mass peaks with a well-known tail decaying over several percent relative to M_0. Analytically, it has been shown that its slope can be evaluated by the factor $a = -C/k_BT$ in log-scale[54]. We can therefore conclude that each individual mass peak represents an image of the energy barrier as a function of the field $Q(F)$ (Supplementary Note 2) and thereby gives information on the early stages of the field evaporation process. Because of the different local atomic environments, the parameter C for the considered atoms varies, leading cumulatively, to mass peaks with slower or faster decay, i.e. with different negative slopes $a = -C/k_BT$ in log-scale[54] (Fig. 1c).

Figure 1 shows a qualitative representation of the field evaporation of an atom departing from four different surface neighborhoods. Since the analysis temperature T is assumed constant during the experiment, the value of C can be directly extracted, for instance here $C_1 > C_2 > C_3 > C_4$ (Fig. 1b).

If the crystal structure is uniform for a pure material (e.g. Supplementary Note 2, Supplementary Fig. 7), the variation of the temperature T leads to a modification of the mass peak slope that is measurable. From the previous data on the pure Al specimen analyzed at 20 to 100 K, we have evaluated the C parameter by using a model to fit the corresponding mass peak shape (Supplementary Note 2). These values were compared with those obtained by the classical experimental method on the same specimen. (Supplementary Note 1, Supplementary Fig. 1). We obtained comparable results of $C = 0.5 \pm 0.1$ eV.

Because Al mainly field evaporates as Al^+ and Al^{2+}, we also measure the slope factor on the Al^{2+} mass peak. In this case, the measurements show a very limited dependence on the charge state, as predicted by the post-ionization theory[55]. The slight difference, <10%, can be explained by dynamic effects caused by the voltage pulse early during the ion flight[56] (Supplementary Note 2).

To verify the robustness of our proposed methodology, we measured the C-value for other pure materials from existing data sets and compared it to the literature. For Ni, we found $C = 0.82 \pm 0.1$ eV. In a recent study from Hatzoglou et al.[12], the C-value of Ni varied from $C = 0.76$ eV in NiCu to $C = 1.17$ eV in FeCrNi, which is consistent with our measurement.

For W, we found $C = 1.8 \pm 0.1$ eV, i.e. slightly lower than the experimental report of Kellogg et al.[52] at 2.2−2.7 eV. The measurement done on the W^{4+} ($C = 1.8$ eV) confirms also the post-ionization theory[55] since are no dynamic effects for this ion mass category[56].

Note that our proposed method of evaluation of this value of the parameter C is dependent on the linearity of the mass peak tail, the level of background towards the base of the mass peak, and the error in the measurement of the specimen's temperature (±10%). We also assumed that the activation energy on the top of the pulse (i.e. $F = F_{EV}$) is 0 eV, whereas it can still range between 0.1 and 0.2 eV, which can induce a shift in the value. We estimate the uncertainty on the measurement of C to be approximately (±10%). However, the approach we have introduced herein has the advantage of being easily applicable to any material analyzed by voltage pulse straight-flight-path APT. It provides a quick and accurate assessment of the field evaporation conditions in a reconstructed dataset.

Local measurement of the parameter *C*. In alloys, the field evaporation process depends on the atoms that constitute the material and on the local atomic organizations, composition, and structures (e.g. Fig. 1), such as precipitates. Thus, the ZBEF of one phase may be higher (or lower) than the other and is closely related to the conventional binding energy of the atoms[8,11,57]. Here we showcase this in the analysis of an AlAg alloy containing Ag-rich precipitates after extracting the mass spectra of the Ag-rich precipitates (Fig. 2a) and Al-rich matrix (Fig. 2b).

Figure 2c shows the mass peaks of Ag^+ from these two regions. As observed, the mass peaks' tail slopes are clearly different. The value of the parameter C is 60% higher in the precipitate than in the matrix. This difference is less visible for Al^+ mass peaks, around 4% higher in the Al-rich matrix (Supplementary Note 3). These observations are complementary to those made in the study of Marquis et al.[8] to explain chromatic aberrations.

We have done similar measurements in the analysis of an AlLi alloy containing Li-rich precipitates[58]. Again, the C-value of Li or Al atoms differ as a function of the local structure (Supplementary Note 3). In these latter measurements, we should consider dynamics effects[56] that influence the measurement by enlarging the Li^+ and Al^{2+} mass peak tails, so that we under-estimate the real C-value of around 10%.

Introducing FEELS: analysis of a structural defect. Since the precision of our measurements of the parameter C is related to a quantity of atoms contained in a mass peak tail, voxelization should allow for measuring the variation of C across an APT volume. This

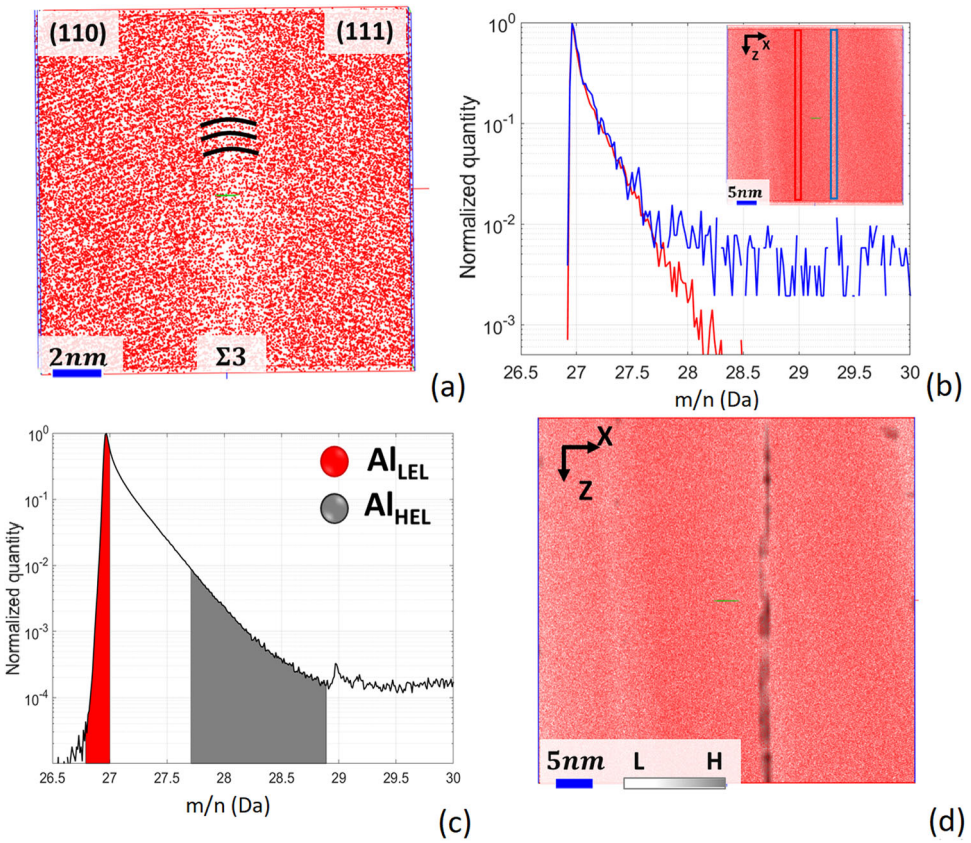

Fig. 3 Experimental measurement of the *C*-value in a Σ3 Al[110](111) analyzed at 60 K. a Reconstructed volume. The grain boundary presents a low density of atoms and a curvy atomic arrangement may be due to rolling-up effects. **b** Al^+ mass peaks associated with the two selected volumes inside the volume: (blue) in the grain boundary, (red) in the crystal. **c** Al^+ mass peak from the volume. (red) Al_{LEL} atoms with low energy loss (LEL) (gray) Al_{HEL} atoms from the tail, with high energy loss (HEL). **d** FEELS representation of the grain boundary after applying a plane projection of the Al_{HEL}/Al_{LEL} composition map to increase visibility. *L* and *H* on the color bar represent respectively Fe_{LEL} and Fe_{HEL}.

simple approach is what we termed as field evaporation energy loss spectroscopy (FEELS). A difference of only tens of atoms between two mass peak tails can be sufficient to reveal a change in *C* by several percent (Supplementary Note 4). Because these measurements are done locally, the data processing algorithms typically used on commercial instruments (i.e. bowl and voltage corrections[9]) do not influence the measurement. However, some errors can appear on the limits of the analyzed volume, i.e. edges of the detector, due to poorer counting statistics.

For a first application, we revisited the APT analysis of a Σ3[110](111) grain boundary, i.e. a region separating two grains of similar crystal structure, in pure Al specimen[59]. In the reconstructed volume (Fig. 3a), the grain boundary is made visible by a lower point density caused by trajectory aberrations[60]. Previous reports on this specific dataset[59] showed no change in composition at the grain boundary itself.

However, the local crystalline structure changes: this special grain boundary exhibits a local hexagonal close-packed structure, whereas the crystal structure of the grains is face-centered cubic, which should lead to different field evaporation behavior as demonstrated by DFT calculations (Supplementary Note 5). To experimentally verify this hypothesis, we plotted the mass spectrum in each of the two regions-of-interest identified in blue and in red in the inset (Fig. 3b). As a result, the slopes are identical over most of the mass peaks, but strongly differ above 27.75 Da, showcasing an increased energy loss for some atoms on the grain boundary. This first result shows, that FEELS is sensitive enough to reveal the difference in the field evaporation process between the grain boundary and the crystal, and can hence image structural defects. These observations corroborated by DFT calculations show a very close correlation between the evolution of $Q(F)$ and the similar evolution of the mass peak tail (Supplementary Note 5 and Supplementary Data).

To visualize the structural changes across the global reconstructed volume, we evaluated the relative quantity of ions contained in the tail, i.e. with a high energy loss denoted Al_{HEL}, and compared it to the rising edge of the mass peak Al_{LEL}, i.e. with a low energy loss (Fig. 3c). Thus, we obtained a FEELS mapping that can be visualized in three-dimensions with a resolution in the nanometer range. In Fig. 3d, we can clearly observe the grain boundary.

Applying FEELS: highlighting structural changes. We now used FEELS on a more complex structure to investigate structural and/or chemical changes. We used an existing data set of a FeBSi metallic glass, crystallized by annealing at 900 °C.[61] After identification of the constituents in the mass spectrum, we reconstructed the volume and extracted mass spectra from a B-rich FeB phase (black mass spectrum) and a Si-rich FeSi phase (gray mass spectrum) from two identically-sized sub-volumes inside each phase (Fig. 4a).

As shown in Fig. 4a the Fe mass peak tails from the two phases appear widely different, evidencing differences in the *C* value and hence field evaporation behavior between the two phases. The FeB phase is crystalline, but field evaporation proceeds experimentally by burst, indicating a complex process of erosion. The rolling-up motion of atoms on the surface of the FeB phase prior to field evaporation may also be more pronounced[11,29]. This is

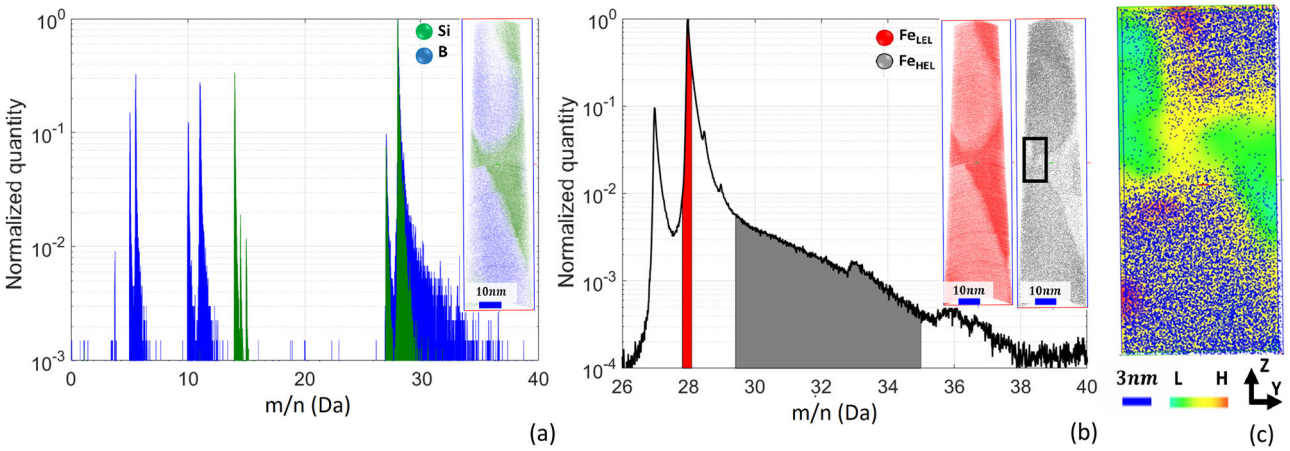

Fig. 4 Experimental measurement of the *C*-value in a FeBSi annealed at 900 °C analyzed at 50 K. a Reconstructed volume: (green) Si in FeSi phase, (blue) B in FeB phase. The corresponding phase mass spectrum is plotted: (green) FeSi phase, (blue) FeB phase. **b** FEELS utilization on Fe^{2+} mass peak of the entire dataset: (red) Fe_{LEL}, (gray) Fe_{HEL}. (Black square) Visualization of the FeSi grain boundary by the FEELS method. The FeB phase and the grain boundary show a high energy loss of Fe. **c** FEELS representation of the FeSi grain boundary in yellow on colormap. The relative concentration of Fe_{HEL} atoms to Fe_{LEL} atoms in the mass spectrum is represented with a color scale. *L* is a low density and *H* is a high density. The grain boundary appears with a medium concentration in yellow. Blue dots represent B atoms in the Fe2B phase.

reflected by the presence of a larger tail of Fe^{2+}, i.e. higher energy loss compared to the FeSi phase, where the field evaporation appears more controlled, as it was observed in FIM[61].

To realize a FEELS mapping of the Fe elements, we consider the Fe mass spectrum of the entire dataset (Fig. 4b and c). We identified Fe from the rising edge of the mass peaks, Fe_{LEL}, Fe from the tail, Fe_{HEL}, and reconstructed the volume. Fe_{LEL} atoms are mostly contained in the FeSi phase; whereas Fe_{HEL} atoms are segregated into the FeB phase (Fig. 4b).

Surprisingly, FEELS also highlights the presence of a grain boundary inside the FeSi phase (Fig. 4c), i.e. enabling to perform structural analysis that can be elusive to conventional APT. FEELS mapping of the complete 3D-reconstructed volume reveals the entire distribution (Supplementary movie 1).

Another example of application on a FeBSi sample annealed for an hour at 500 °C is presented in Supplementary Note 6. In this experiment, we expected two crystalline phases FeSi and FeB, however, FEELS reveals a third phase. The composition measurement shows no distinction with a FeB phase, so we believe that the crystalline structure is locally different. Further studies are underway to verify this hypothesis.

Conclusion

In the first part, we demonstrated that the mass peaks in APT are not only useful to identify and quantify elements in the analysis, but their shape encodes information regarding the binding of an atom with its neighborhood and energetic aspects related to the field evaporation process. The measurement of the slope of the mass peak tails allows us to extract easily the parameter *C*.

With this methodology, a database can already be started and populated by revisiting existing analyses. This will help to confirm and compare the different values found from further ongoing DFT studies. In the configuration of the state-of-the-art instruments (LEAP 5000XS), measurements are reliable for a wide range of elements with a mass-to-charge ratio above ~15 Da, below which the dynamic effects associated with the voltage pulse amplify the error. It should be improved by reconsidering the dynamic effects in the mass spectra optimization algorithms or by reducing the dynamic effects by coupling the voltage pulse to the tip as was proposed previously[56]. Optimization of the *C*-value measurement should be possible by tabulating mass peak enlargements associated with the voltage pulse fraction and DC Voltage amplitude.

In the second part, we introduced FEELS to map changes in *C*-value at the nanoscale. We have showcased the possibility to discriminate between phases, i.e. precipitates in a matrix, between structural defects and their surroundings, and enabling to reveal of microstructural details that were elusive to conventional APT analysis, such as a grain boundary. FEELS offers wide possibilities to revisit and complement conventional APT analyses, in particular in search for possible microstructural features, particularly structural defects, that had remained hidden within existing data and could hence be targeted for structural and compositional analyses. We expect to achieve detection of dislocations or defects such as vacancy clusters for instance.

For the moment, our approach is only amenable for voltage pulse straight-flight-path APT analysis, but further studies are already engaged to investigate possibilities to apply the method to reflectron-fitted atom probes. Indeed the ion time-of-flight dispersion induced by the energetic distribution in these instruments is simply reduced[2]. It means the information is still present but first-order energy deficits are transformed into second-order terms, making them more difficult to be evaluated and analyzed. A post-processing method could aim to deconvolute this compression to retrieve the parameter *C*. This also means that mass spectra of materials requiring laser pulse APT mode could be analyzed and explored using coupled voltage/laser pulsing modes that are available in the latest generation of atom probes[62] opening the FEELS to a wider range of applications.

Methods

The pure tungsten specimen was prepared from a wire oriented, along the ⟨011⟩ direction, and prepared by electrochemical polishing with a solution of 5% NaOH in water with a voltage in the range of 1−5 V. Pure Al specimen was prepared using an electropolishing method with 1−10% perchloric acid in methanol with a voltage in the range of 5−8 V. Pure Ni specimen was prepared using an electropolishing method with 10% perchloric acid 70%, 20% glycerol in ethanol. The final step is done with 2% perchloric acid in 2-butoxyethanol. The voltage range is 22*V*. Further details on the electropolishing method can be found in the literature[14,23,63].

The Σ3[110](111) grain boundary volume comes from a pure Al (>99.99%) used to form bi-crystals via the Bridgman technique. The crystals were sectioned using a diamond wire saw into rectangular blocks that were 3 mm long, 1 mm wide, and 500 µm thick. The grain boundary was placed end on when looking at the 3 × 1 mm face, and 45° away from the longest axis of the block. One 3 × 1 mm face was mechanically polished for a few tens of microns using 1200 and then 4000 grit SiC paper. The block was then dipped into an aqueous solution of HNO_3, HCl, and HF to optically reveal the GB. Further information can be found in ref. [59].

The AlAg alloy was prepared with Al−3 at.% Ag aged at 300 °C for 3 min, which produced 8–15-nm-diameter GP zones containing 34 at.% Ag. The specimens were prepared using standard electropolishing solutions. Further information can be found in ref. [8].

The AlLi alloy was annealed for 8 h at 500 °C. The needle-shaped specimens were then fabricated by electropolishing in a solution of 25% perchloric acid in glacial acetic acid with a 10−12 V_{DC}, followed by a second stage of fine polishing under a binocular microscope with 2% perchloric in 2-butoxyethanol with a 20−25 V_{DC}. Further information can be found in ref. [64].

The FeBSi metallic glass alloy's initial composition is 77.5% of Fe, 15% of B, and 7.5% of Si. The specimen originally presents an amorphous structure that was crystallized at 500 or 900 °C for an hour. Needle shape specimens were prepared by focused ion beam (FIB) preparation using a xenon plasma-focused ion beam instrument[14,23,63].

Atom Probe experiments were done using a straight flight path LEAP series[62] in classical conditions. The voltage pulse fraction was 15% or 20% and the applied temperature was under 100 K.

Data availability

The data that support the findings of this study are available from the corresponding authors upon reasonable request.

Received: 30 May 2022; Accepted: 6 April 2023;
Published online: 10 May 2023

References

1. Brandon, D. G. On field evaporation. *Philos. Mag.* **14**, 803–820 (1966).
2. Pareige, C., Lefebvre-Ulrikson, W., Vurpillot, F. & Sauvage, X. Time-of-flight mass spectrometry and composition measurements. In *Atom Probe Tomography* (eds Lefebvre-Ulrikson, W., Vurpillot, F. & Sauvage, X.) Ch. 5, 123–154 (Academic Press, 2016).
3. Gault, B. et al. Atom probe tomography. *Nat. Rev. Methods Prim.* **1**, 52 (2021).
4. Haley, D., London, A. J. & Moody, M. P. Processing APT spectral backgrounds for improved quantification. *Microsc. Microanal.* **26**, 964–977 (2020).
5. Miller, M. K. The effects of local magnification and trajectory aberrations on Atom Probe analysis. *J. Phys. Colloq.* **48**, C6–565–C6–570 (1987).
6. Waugh, A., Boyes, E. & Southon, M. Investigations of field evaporation with a field-desorption microscope. *Surf. Sci.* **61**, 109–142 (1976).
7. Vurpillot, F., Bostel, A. & Blavette, D. Trajectory overlaps and local magnification in three-dimensional atom probe. *Appl. Phys. Lett.* **76**, 3127–3129 (2000).
8. Marquis, E. A. & Vurpillot, F. Chromatic aberrations in the field evaporation behavior of small precipitates. *Microsc. Microanal.* **14**, 561–570 (2008).
9. Larson, D., Gault, B., Geiser, B., De Geuser, F. & Vurpillot, F. Atom probe tomography spatial reconstruction: status and directions. *Curr. Opin. Solid State Mater. Sci.* **17**, 236–247 (2013).
10. Miller, M. K. & Smith, G. D. W. An atom probe study of the anomalous field evaporation of alloys containing silicon. *J. Vac. Sci. Technol.* **19**, 57–62 (1981).
11. Oberdorfer, C. et al. Influence of surface relaxation on solute atoms positioning within atom probe tomography reconstructions. *Mater. Charact.* **146**, 324–335 (2018).
12. Hatzoglou, C. et al. Preferential evaporation in atom probe tomography: an analytical approach. *Microsc. Microanal.* **26**, 689–698 (2020).
13. Miller, M. & Hetherington, M. Local magnification effects in the atom probe. *Surf. Sci.* **246**, 442–449 (1991).
14. Gault, B. (ed.) *Atom Probe Microscopy*. No. 160 *in Springer Series in Materials Science* (Springer, New York, 2012).
15. Yao, L., Withrow, T., Restrepo, O. D., Windl, W. & Marquis, E. A. Effects of the local structure dependence of evaporation fields on field evaporation behavior. *Appl. Phys. Lett.* **107**, 241602 (2015).
16. Vurpillot, F. & Oberdorfer, C. Modeling atom probe tomography: a review. *Ultramicroscopy* **159**, 202–216 (2015).
17. De Geuser, F. & Gault, B. Metrology of small particles and solute clusters by atom probe tomography. *Acta Mater.* **188**, 406–415 (2020).
18. Gault, B. et al. Reflections on the spatial performance of atom probe tomography in the analysis of atomic neighborhoods. *Microsc. Microanal.* 1–11, https://www.cambridge.org/core/product/identifier/S1431927621012952/type/journal_article (2021).
19. Vurpillot, F., Bostel, A., Cadel, E. & Blavette, D. The spatial resolution of 3D atom probe in the investigation of single-phase materials. *Ultramicroscopy* **84**, 213–224 (2000).
20. Vurpillot, F., Da Costa, G., Menand, A. & Blavette, D. Structural analyses in three-dimensional atom probe: a Fourier transform approach. *J. Microsc.* **203**, 295–302 (2001).
21. Gault, B. et al. Spatial resolution in atom probe tomography. *Microsc. Microanal.* **16**, 99–110 (2010).
22. Forbes, R. G. Field evaporation theory: a review of basic ideas. *Appl. Surf. Sci.* **87-88**, 1–11 (1995).
23. Miller, M. K. & Forbes, R. G. *Atom-Probe Tomography* (Springer US, Boston, MA, 2014).
24. Suchorski, Y., Ernst, N., Schmidt, W. A., Medvedev, V. K., Kreuzer, H. J., Wang, R. L. C. Field desorption and field evaporation of metals: In memoriam Professor J.H. Block. *Progress in Surface Science*. **53**, 135–153 (1996).
25. Boll, T., Zhu, Z.-Y., Al-Kassab, T. & Schwingenschlögl, U. Atom probe tomography simulations and density functional theory calculations of bonding energies in Cu_3Au. *Microsc. Microanal.* **18**, 964–970 (2012).
26. Boll, T. & Al-Kassab, T. Interpretation of atom probe tomography data for the intermetallic TiAl+Nb by means of field evaporation simulation. *Ultramicroscopy* **124**, 1–5 (2013).
27. Ernst, N. Experimental investigation on field evaporation of singly and doubly charged rhodium. *Surf. Sci.* **87**, 469–482 (1979).
28. Forbes, R. G., Chibane, K. & Ernst, N. Derivation of bonding distance and vibration frequency from field evaporation experiments. *Surf. Sci.* **141**, 319–340 (1984).
29. Zhu, M. et al. Unique bond breaking in crystalline phase change materials and the quest for metavalent bonding. *Adv. Mater. (Deerfield Beach, Fla.)* **30**, e1706735 (2018).
30. Yu, Y., Cagnoni, M., Cojocaru-Mirédin, O. & Wuttig, M. Chalcogenide thermoelectrics empowered by an unconventional bonding mechanism. *Adv. Funct. Mater.* **30**, 1904862 (2020).
31. Raghuwanshi, M., Cojocaru-Mirédin, O. & Wuttig, M. Investigating bond rupture in resonantly bonded solids by field evaporation of carbon nanotubes. *Nano Lett.* **20**, 116–121 (2020).
32. Herbig, M. Spatially correlated electron microscopy and atom probe tomography: current possibilities and future perspectives. *Scr. Mater.* **148**, 98–105 (2018).
33. Mancini, L. et al. Carrier localization in GaN/AlN quantum dots as revealed by three-dimensional multimicroscopy. *Nano Lett.* **17**, 4261–4269 (2017).
34. Prakash, A. et al. Atom probe informed simulations of dislocation–precipitate interactions reveal the importance of local interface curvature. *Acta Mater.* **92**, 33–45 (2015).
35. Ramasse, Q. M. et al. Probing the bonding and electronic structure of single atom dopants in graphene with electron energy loss spectroscopy. *Nano Lett.* **13**, 4989–4995 (2013).
36. Hawkes, P. W. & Spence, J. C. H. (eds) *Springer Handbook of Microscopy. Springer Handbooks* (Springer, Cham, 2019).
37. Deconihout, B., Menand, A., Bouet, M. & Sarrau, J. Performance of an energy compensated time-of-flight mass spectrometer. *Surf. Sci.* **266**, 523–528 (1992).
38. Scheinfein, M. R. & Seidman, D. N. Time aberrations of uniform fields: an improved reflectron mass spectrometer for an atom-probe field-ion microscope. *Rev. Sci. Instrum.* **64**, 3126–3131 (1993).
39. Cerezo, A., Godfrey, T. J., Sijbrandij, S. J., Smith, G. D. W. & Warren, P. J. Performance of an energy-compensated three-dimensional atom probe. *Rev. Sci. Instrum.* **69**, 49–58 (1998).
40. Bémont, E. et al. Effects of incidence angles of ions on the mass resolution of an energy compensated 3D atom probe. *Ultramicroscopy* **95**, 231–238 (2003).
41. Müller, E. W. & Krishnaswamy, S. Energy deficits in pulsed field evaporation and deficit compensated atom-probe designs. *Rev. Sci. Instrum.* **45**, 1053–1059 (1974).
42. Poschenrieder, W. Multiple-focusing time of flight mass spectrometers Part I. Tofms with equal momentum acceleration. *Int. J. Mass Spectrom. Ion-. Phys.* **6**, 413–426 (1971).
43. Poschenrieder, W. Multiple-focusing time-of-flight mass spectrometers Part II. TOFMS with equal energy acceleration. *Int. J. Mass Spectrom. Ion-. Phys.* **9**, 357–373 (1972).
44. Muller, E. W. Field desorption. *Phys. Rev.* **102**, 618–624 (1956).
45. Sánchez, C., Lozovoi, A. & Alavi, A. Field-evaporation from first-principles. *Mol. Phys.* **102**, 1045–1055 (2004).
46. Freysoldt, C., Mishra, A., Ashton, M. & Neugebauer, J. Density Functional Modelling of Field Evaporation https://www.nist.gov/system/files/documents/2018/05/01/aptm_2018_freysoldt.pdf (2018).
47. Ono, T. & Hirose, K. First-principles study on field evaporation for silicon atom on Si(001) surface. *J. Appl. Phys.* **95**, 1568–1571 (2004).
48. Ashton, M., Mishra, A., Neugebauer, J. & Freysoldt, C. Ab initio description of bond breaking in large electric fields. *Phys. Rev. Lett.* **124**, 176801 (2020).
49. Ohnuma T. First-Principles Calculation of the Evaporation Field and Roll-up Effect of M (M = Fe, Cu, Si, and Mn) on the Fe (001) and Fe Step Structure. *Microsc Microanal.* **28**, 1181–1187 (2022).
50. Forbes, R. G. An alternative theoretical approach to field evaporation rate sensitivities. *Surf. Sci.* **46**, 577–601 (1974).

51. Wada, M. On the thermally activated field evaporation of surface atoms. *J. Phys. Colloq.* **45**, C9–89–C9–94 (1984).
52. Kellogg, G. L. Measurement of activation energies for field evaporation of tungsten ions as a function of electric field. *Phys. Rev. B* **29**, 4304–4312 (1984).
53. Vurpillot, F. Three-dimensional reconstruction in atom probe tomography: basics and advanced approaches. In *Atom Probe Tomography* (eds Lefebvre-Ulrikson, W., Vurpillot, F. & Sauvage, X.) Ch. 7, 183–249 (Academic Press, 2016).
54. Zhao, L., Normand, A., Delaroche, F., Ravelo, B. & Vurpillot, F. Pulse shaping optimization for improving atom probe tomography. *Int. J. Mass Spectrom.* **386**, 47–53 (2015).
55. Kingham, D. R. The post-ionization of field evaporated ions: a theoretical explanation of multiple charge states. *Surf. Sci.* **116**, 273–301 (1982).
56. Rousseau, L. et al. Dynamic effects in voltage pulsed atom probe. *Microsc. Microanal.* 1–14, https://www.cambridge.org/core/product/identifier/S1431927620024587/type/journal_article (2020).
57. Ge, X.-j., Chen, N.-x., Zhang, W.-q. & Zhu, F.-w. Selective field evaporation in field-ion microscopy for ordered alloys. *J. Appl. Phys.* **85**, 3488–3493 (1999).
58. Gault, B. et al. Atom probe microscopy investigation of Mg site occupancy within δ' precipitates in an Al–Mg–Li alloy. *Scr. Mater.* **66**, 903–906 (2012).
59. Wei, Y. et al. 3D nanostructural characterisation of grain boundaries in atom probe data utilising machine learning methods. *PLoS ONE* **14**, e0225041 (2019).
60. Oberdorfer, C., Eich, S. M. & Schmitz, G. A full-scale simulation approach for atom probe tomography. *Ultramicroscopy* **128**, 55–67 (2013).
61. Klaes, B. et al. Analytical three-dimensional field ion microscopy of an amorphous glass FeBSi. *Microsc. Microanal.* 1–9, https://www.cambridge.org/core/product/identifier/S1431927621012629/type/journal_article (2021).
62. CAMECA, 2020. https://www.cameca.com (2020).
63. Blum, I., Cuvilly, F. & Lefebvre-Ulrikson, W. Atom probe sample preparation. In *Atom Probe Tomography* (eds Lefebvre-Ulrikson, W., Vurpillot, F. & Sauvage, X.) 97–121 (Elsevier, 2016).
64. Gault, B. et al. Atom probe microscopy investigation of Mg site occupancy within δ' precipitates in an Al–Mg–Li alloy. *Scr. Mater.* **66**, 903–906 (2012).

Acknowledgements

We thank Uwe Tezins, Christian Broß, and Andreas Sturm for their support of the FIB and APT facilities at MPIE. L.T.S. and B.G. acknowledge financial support from the ERC-CoG-SHINE-771602. F.F.M. acknowledges financial support from the International Max Planck Research School for Interface Controlled Materials for Energy Conversion (IMPRS-SurMat). F.V. acknowledges the support of the French Agence Nationale de la Recherche (ANR), under grant ANR-21-CE42-0024 (project HiKEAP).

Author contributions

L.R. realized and interpreted all the experimental data processing and the simulations of the dynamic effects to develop the FEELS method. He wrote the manuscript. A.N. helped to carry out the interpretations of the experimental data processing and the simulations of the dynamic effects to develop the FEELS method. F.F.M. and L.T.S. produced the experimental data for FeBSi points annealed at 500 and 900 °C. H.-S.M.S.S. and C.H., and G.D.C. have contributed to the interpretation of the experimental data to develop the FEELS method. K.T. supervised this research and contributed to the interpretation of the results. C.F. performed the DFT calculations for Al and contributed to the interpretation of the results to develop the FEELS method. B.G. and F.V. supervised this research and contributed to the interpretation of the results, as well as to the writing of the article.

Competing interests

The authors declare no competing interests.

Additional information

Supplementary information The online version contains supplementary material available at https://doi.org/10.1038/s42005-023-01203-2.

Correspondence and requests for materials should be addressed to Loïc Rousseau.

Peer review information *Communications Physics* thanks Richard Forbes, Julie Cairney and the other, anonymous, reviewer(s) for their contribution to the peer review of this work. Peer reviewer reports are available.

Reprints and permission information is available at http://www.nature.com/reprints

Publisher's note Springer Nature remains neutral with regard to jurisdictional claims in published maps and institutional affiliations.